Pulp fibre foams: Morphology and mechanical performance

Citation for the original published paper (version of record):
Wagner, M., Biegler, V., Wurm, S. et al (2025). Pulp fibre foams: Morphology and mechanical performance. Composites Part A: Applied Science and Manufacturing, 188.
http://dx.doi.org/10.1016/j.compositesa.2024.108515

Composites: Part A 188 (2025) 108515

Contents lists available at ScienceDirect

Composites Part A

journal homepage: www.elsevier.com/locate/compositesa

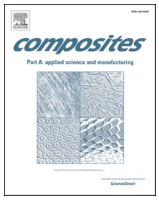

Pulp fibre foams: Morphology and mechanical performance

Markus Wagner [a,1], Veronika Biegler [b,1], Sebastian Wurm [a], Georg Baumann [a], Tiina Nypelö [d,e], Alexander Bismarck [b,c], Florian Feist [a,*]

[a] Vehicle Safety Institute, Graz University of Technology, Inffeldgasse 13/6, 8010 Graz, Austria
[b] Institute of Materials Chemistry, Faculty of Chemistry, University of Vienna, Währinger Straße 42, 1090 Vienna, Austria
[c] Department of Chemical Engineering, Imperial College London, South Kensington Campus, London SW7 2AZ, United Kingdom
[d] Department of Chemistry and Chemical Engineering, Chalmers University of Technology, Kemigården 4, 412 58 Gothenburg, Sweden
[e] Department of Bioproducts and Biosystems, Lignocellulose Chemistry, Aalto University, Puunjalostustekniikka 1, 00076 AALTO, Finland

ARTICLE INFO

Keywords:
Fibre foams
Cellulose
Production
Mechanical properties
Morphology

ABSTRACT

Cellulose (pulp) fibre foams serve as bio-based alternative to fossil-based cellular lightweight materials. The mechanical properties of cellulose fibre foams are inferior compared with traditional polymer foams and available information is often limited to compression properties. We present a comprehensive analysis of cellulose fibre foams with densities ranging from 60 to 130 kg/m^3, examining their compression, tensile, flexural, and shear properties. Key findings include a high mean zenithal fibre angle which decreases with increasing density, as well as a high strain rate amplification (SRA) in compressive strength, which also decreases with increasing density. With respect to formulation, the addition of carboxymethyl cellulose (CMC) enhanced fibre dispersion, bubble homogeneity of the wet foam, and dimensional stability of the end-product.

These results provide a foundation for numerical models and advance the understanding of cellulose pulp fibre foams, highlighting their potential for certain applications.

1. Introduction

The demand for lightweight materials for various structural, thermal, and acoustic insulation applications is pertinent and driven by the need for improved energy efficiency achieved by lightweighting [1]. Lightweighting is currently realised by the utilization of polymer or metal foams either on their own or as core material in sandwich composites. Structural foams are attractive because of their high specific strength, energy absorption potential, and favourable (thermal and acoustic) insulation properties [2–4]. The environmental impact associated with these foam materials, includes significant CO_2 emissions during production, raw material scarcity, and the generation of microplastics at the end of their lifecycle, which prompted an increased interest in sustainable alternatives [5,6]. While fossil-based foams offer ease of production and cost-effectiveness, particularly for packaging and low-cost structural applications, the pursuit for sustainable alternatives has led to the exploration of mycelium-based composites [7], pressed non-woven plant fibre materials [8], and cellulosic fibre foams manufactured as potential eco-friendly alternatives [9].

Pulp fibre foams have received significant interest [10–12]. The production of porous materials directly from cellulose pulp fibres offers a cost-effective alternative to structural foams. Pulp fibres with dimensions of 1–3 mm in length and 15–28 μm in diameter [13], depending on their origin, often serve as raw material for production of microfibrillated cellulose (MFC) and cellulose nanofibrils (CNF) by mechanical, chemical (HCl hydrolysis) or enzymatic disintegration [14]. Nanocellulose-based foams account for a large proportion of cellulose foams [15]. However, the costly production of CNF requiring high energy input renders them an economically unfavourable solution to replace low-cost polymer foams [16].

Pulp fibre foams are commonly produced by incorporating air into aqueous fibre suspensions containing suitable surfactants to stabilise the liquid froth. The fibre froth is moulded, the suspension medium drained and the froth dried, resulting in pulp fibre foams with adjustable

Abbreviations: CMC, carboxymethyl cellulose; SRA, strain rate amplification; MFC, microfibrillated cellulose; CNF, cellulose nanofibrils; CTMP, chemi-thermo-mechanical-pulp; BSKP, bleached softwood kraft pulp; SR, Schopper Riegler; SDS, sodium dodecyl sulphate; SEM, scanning electron microscopy; μCT, micro-computed tomography; EPS, expanded polystyrene; EPP, expanded polypropylene.

* Corresponding author.
E-mail address: florian.feist@tugraz.at (F. Feist).

[1] Authors contributed equally.

https://doi.org/10.1016/j.compositesa.2024.108515
Received 5 August 2024; Received in revised form 25 September 2024; Accepted 7 October 2024
Available online 9 October 2024

properties depending on the additives used [10,17–20]. Additives are used to improve the common issues of cellulose based materials, such as their flammability [20,21], hydrophilicity [18] and poor mechanical properties of low-density foams [20,22]. Foam materials are mainly characterised by their mechanical properties under compression, in addition to their density and morphology. The behaviour of fibrous foams in compression has been intensively studied [11] to determine their modulus and strength, with a view to optimizing the structure of fibre networks. Ketoja et al. [23] described the failure mechanism of well-bonded 3D networks (foams) of chemi-thermomechanical-pulp (CTMP), bleached softwood kraft pulp (BSKP) and a weakly bonded network formed by viscose and CNF. They state that under compressive loading, the central deformation mechanism is fibre buckling. A lower foam density, implying a longer segment length with fewer inter-fibre crossings, results in weaker structural response. If fibre segments are not strengthened by other fibres, the structure cannot withstand applied loads. To gain further insights into the mechanical response of bonded fibre networks, Bergström et al. [24] studied uniaxial compression of non-bonded air-laid southern pine pulp fibres networks. The synergistic effect of fibres bonded via elasto-plastic contacts and fibre–fibre adhesion led to greater non-reversible deformations compared to networks comprising only elasto-plastic fibre contacts. Pöhler et al. [22] produced BSKP and hemp fibre networks bonded with polymeric additives (locust bean gum and polyvinyl alcohol), CNF, and paper fines. Their primary objective was to enhance fibre–fibre bond strength, particularly by increasing the inter-fibre contact areas. Polymeric components, particularly polyvinyl alcohol, were shown to provide the most significant strength improvements. Measured compression properties deviated from theoretical predictions made using Sampson's unified theory for statistics of flocculated and random fibre networks [25]. While such approaches based on Sampson's theory show promise, further refinement is necessary to enhance their accuracy and reliability. Carboxymethyl cellulose (CMC) is a cellulose derivate from various hard- and softwood sources. Its thickening, stabilizing, and film-forming properties makes it a favourable additive in the textile and paper industries [26,27]. CMC is also commonly used as additive to enhance the texture of gluten-free bread. Due to CMC's physiological inertness, CMC is regarded to be generally safe to end-users and the environment. CMC was reported to enhance the strength of hand sheets [28], which makes it a prime candidate to use as polymeric additive to improve the strength of pulp foams [22].

We provide a comprehensive mechanical evaluation of pulp fibre foams containing a bio-based polymeric binder with a wide range of densities under various loading conditions. We report essential compression, tension, bending, and shear properties along with structural characteristics, such as pore and fibre orientation, across a wide range of densities. The data provided enable the suitability assessment of such foams for a variety of applications, with emphasis on structural applications in mechanical and civil engineering, and the sports/leisure industry. Besides static mechanical properties we also investigate the high strain rate response of pulp fibre foams, closing the gap in literature shown by Pääkkönen et al. [29] and offering novel insights crucial for impact applications relevant to packaging, energy-absorbing automotive parts, or personal safety equipment such as impact liners for helmets. We provide data that will facilitate the generation of material models suitable for both quasi-static evaluations and dynamic load cases, hence enabling their future adoption.

2. Methods

2.1. Pulp and chemicals

Once dried bleached softwood kraft pulp sheets (BSKP) of a composition of 85 % spruce, 10 % pine, and 5 % larch were kindly provided by Zellstoff Pöls AG (Austria). The Schopper Riegler (SR) for all samples was determined according to TAPPI standard T 227 to be 11.3 $\pm$ 1.2 SR. The fibre length (length weighted average, l_f) was determined using the L&W Fibre Tester Plus, ABB (Switzerland) in the wet state (Table S1). Sodium-carboxymethylcellulose (CMC, MW 250 000) and the anionic surfactant sodium dodecyl sulphate (SDS, $\geq$ 99 %) were purchased from Sigma Aldrich and used as received.

2.2. Manufacturing of pulp fibre foams

The pulp sheets were dispersed according to TAPPI standard T-200: m in a valley beater (FRANK PTI, Germany). After the dispersion process in the valley beater, aqueous pulp fibre solutions were dewatered to pulp fibre content of 10 wt%. CMC (5 wt% in water) functioning as a viscosity modifier and dispersing agent in the wet foam, was mixed using a kitchen mixer equipped with a whisking head (1000 W, Kenwood, UK). Before frothing, SDS (0.5 wt% with respect to the dry fibre weight) was added. Depending on the desired density, the pulp solution was frothed until the target density was reached. After frothing, the fibre froth was transferred into an open polyoxomethylene mould (310 mm (x), 310 mm (y), and 20 mm (z). During production, gravity acts in the negative z direction.) and dried in a laboratory oven at 80 °C for 8–12 h. The foam was considered dry when a moisture content below 10 wt% was reached. The foam plates were stored at ~25 °C at ~40 %RH prior to characterisation.

2.3. Foam morphology

Scanning electron microscopy (SEM) (JCM-6000, JEOL, Germany) was used to investigate the foam morphology. The SEM was operated at an acceleration voltage of 10 kV using a secondary electron detector. Prior to imaging, all samples were fixed with carbon tape to a sample holder and gold-coated using a sputter coater (JEOL Fine Coater JFC-1200, Germany) for 40 s at 30 mA.

Micro-computed tomography (μCT) scans were performed using an UMITOM XL (Tescan). Specimens with densities of 60 and 130 kg/m^3 were produced by cutting a cylindrical shape with a diameter of 20 mm from a foam panel 20 mm in height. To ensure stable mounting and prevent image blur, specimens were securely housed in thin-walled 3D-printed PLA sample holders with a tight fit. The spatial scan resolution was set to 15 μm, aligning closely with the recommended 1/1000 ratio for sample and voxel size [29 30]. To generate a scan of the complete specimen, it was necessary to perform three partial scans and stitch them together after the acquisition process. A scan voltage of 40 kV and a current of 375 μA were utilized over an acquisition time of ~70 min. No spectral filter was employed during scanning to produce pictures with high contrast. The resulting three-dimensional datasets were analysed using the Dragonfly software, Version 2022.2 (Build 1409) for Windows (Comet Technologies Canada Inc., Montreal).

Pore size was assessed by manual thresholding. Isolated islands with fewer than nine voxels and one- or two-voxel thick voids were excluded to avoid false identification of pores, resulting in a minimal pore size of 30 μm. These small free spaces between fibres represent voids rather than pores templated by air bubbles and where therefore disregarded. The segmented data was analysed using the "PoreSpy" [31] and "OpenPNM" [32] software plug-ins, both utilize the Snow algorithm developed by Gostick [33]. Various pore metrics were evaluated, including pore volume V_p, the mean Sauter diameter d_{32}, the maximum Feret diameter F, which represents the largest extent of a pore [34], and the sphericity Ψ. Sphericity describes the ratio of the surface area of an ideal spherical pore, based on the measured pore volume (V_p), to the estimated pore surface area (A_p) from the μCT measurement (Eq. (1). A value of Ψ equal to 1 represents a perfectly sphere-shaped pore.

$$\Psi = \frac{\left(6\pi^{\frac{1}{2}} V_p\right)^{\frac{2}{3}}}{A_p} \quad (1)$$

Fibre orientation was assessed using a an in-house developed Python tool. This tool applies Gaussian smoothing to the three-dimensional greyscale data sets. Skeletonization was then performed, using the "skimage" python library [35] and the Hessian matrix was calculated for each remaining filled voxel. The local orientation of each voxel was derived from the eigenvalues of the corresponding Hessian matrices. A similar approach, based on the greyscale values with an subsequent evaluation of their second derivative, has already been proposed by Frangi et al. [36] It was shown that the orientation of the fibre network can be derived with reasonable accuracy even when the fibre diameter is smaller than the resolution of the μCT scan [37].

Relative density was assessed by dividing the envelope density ρ^* by the skeletal density ρ_s. The envelope density was determined by the ratio of foam weight and volume. The skeletal density was measured using helium-pycnometry (Micrometics AccuPyk) to be $\rho_s = 1449 \pm 3$ kg/m^3 and the porosity ϕ calculated by Eq. (2) [4]:

$$\phi = 1 - \frac{\rho^*}{\rho_s} \tag{2}$$

Density distribution was determined utilizing segmented data to correlate scan data and ρ^* [38]. The dataset segmented by manual thresholding, without further modifications such as island processing, was used. Each filled voxel was assigned a weight such that the sum of all voxels equalled the specimen weight. The assigned voxel weights varied among different specimens. This variability was crucial due to the relative scale of the greyscale data for each specimen. The highest brightness value was assigned to the maximum x-ray absorption, while the minimum absorption was set to zero. Consequently, manual thresholding and individual voxel weight assignment were required for each specimen. The density distribution was analysed in the x, y, and z directions resulting in a density distribution along each main axis.

2.4. Mechanical properties

Quasi-static mechanical tests were performed using a universal testing machine (UTM Z020, ZwickRoell). The machine was equipped with 20 kN load cell with an accuracy class of 0.2 %. The experiments were carried out at 20 °C, about 70 %RH (Remark: Aimed RH was 65 %, as proposed for testing of wood-products, e.g. EN 319:1993).

Uniaxial compression tests were performed following standard ISO 844. The testing speed was 5 mm/min, resulting in a strain rate of 0.0042 s^{-1}. At least five specimens were tested for each configuration. A pre-force of 2 N was been applied prior to testing and the measurement ended when a force level of 15 kN was reached. Engineering stress over engineering strain curves were generated. Foam specimens were tested in out-of-plane (force applied in foam production height direction, i.e. z direction) and in-plane orientations (force applied perpendicular to the height direction, i.e. in the xy-plane). The out-of-plane specimens were 50 × 50 × 20 mm plates and the in-plane specimens were 20 × 20 × 20 mm cubes (Figure S1).

The densification strain was determined using the tangential method, which was also used by Li et al. [39]. This method defines the densification strain as the intersection point of the tangents to the "stress plateau" region and to the densification region.

The mean crush strength σ_m, an indicator for the energy absorption capacity, was obtained as follows:

$$\sigma_m = \frac{1}{\varepsilon_D}\int_0^{\varepsilon_D} \sigma_{(\varepsilon)} d\varepsilon \tag{3}$$

where ε_D is the densification strain and $\sigma_{(\varepsilon)}$ the stress at any given strain. The amount of energy absorbed E_A was determined by integrating the area underneath the force–displacement curve:

$$E_A = \int_0^s F_{(s)} ds \tag{4}$$

where $F_{(s)}$ is the force dependent on the displacement s. The specific energy absorption SEA enables comparison between different foam structures and is the ratio of E_A of a certain structure and its mass m:

$$SEA = \frac{E_A}{m} \tag{5}$$

Tensile tests were performed at a test speed of 20 mm/min according to standard ISO-1926 on five dog bone shaped specimens (Figure S2). Test specimens had a length of 150 mm (x direction), with a gauge length of 55 mm and a width (y direction) of 25 mm and a height (z direction) of 20 mm. The ends of the test specimens were coated with a highly viscous epoxy resin (Uhu Endfest 300) and a casting epoxy resin (Greenpoxy) to ensure clamping without compressing the material in the jig. The specimens were pre-loaded with 2 N and tests ended after a 95 % decline in force was detected. Tensile strengths and moduli were determined from engineering stress–strain curves. To validate the modulus calculated from the traverse displacement the strain was also recorded using a video-extensometer for selected samples.

Flexural tests were performed in three-point bending following standard ISO 1209–2. The setup consisted of two half-cylindrical supports with a diameter of 30 mm separated by 240 mm and a half-cylindrical impactor moving at 20 mm/min. Prior to testing a preload of 2 N was applied. The test ended when the force dropped by 95 % from its peak or after reaching a displacement s of 60 mm. Test specimens had dimensions of 290 × 40 × 20 mm with the force being applied in the z direction of the foam. Drying of wet foams caused the formation of a skin on the open mould side, for this reason two different configurations were tested for each density group: one in which the skin layer is in contact with the impactor (4 specimens/density) and one perpendicular to it (3 specimens/density).

Force-displacement curves were used to calculate the energy absorption capacity using Eqs. (6) and (7) [40]. The flexural modulus E was calculated as follows:

$$E = \frac{L^3 F}{48 I s} \tag{6}$$

$$I = \frac{B H^3}{12} \tag{7}$$

where L is the span length, F the measured force, I the second moment of area, s the displacement, H the specimen height, and B the specimen width.

Double lap shear tests were performed following standard ISO-1922. Two foam panels measuring 240 × 50 × 20 mm (x, y and z direction, respectively) were adhesively bonded to three parallel poplar plywood plates with 8 mm thickness and 5 ply's each. (Figure S3). This test configuration represents an out-of-plane shear load case. The two outer plates are connected to a plywood block acting as spacer. Tests were performed at a speed of 20 mm/min following pre-loading of 2 N. The experiment ended when a 95 % force drop was detected. For each specimen, the relative displacement of each support was measured using Blender (version 2.79b) target tracking. From the relative displacements of the supports, the mean engineering shear strain γ of 4 locations was calculated as follows [41]:

$$\gamma = \frac{\sum_{k=1}^{n=4} \left(\frac{\Delta x_k}{z_0}\right)}{n} \tag{8}$$

where Δx is the measured displacement and z_0 the height of the specimen. The output force–time curve was used to calculate the engineering shear stress, which was used to produce the shear stress–strain curve. The shear modulus has also been assessed by Eq. (9) for the initial linear

region.

$$G = \frac{F/A}{\gamma} \tag{9}$$

Tests were performed in triplicate. The low number of repetitions was justified due to the large shear area per test and that each specimen consisted of two separate foam panels.

Dynamic out-of-plane compression tests were performed using a universal Split Hopkinson bar [42,43]. Besides the stress–strain signal derived from the strain-gauges on the bar-system a high-speed camera (Phantom Veo 640) was used at a frame-rate of 50 kfps to track the deformation behaviour of the foam specimen. Cylindrical samples with a diameter and height of roughly 20 mm and densities of 60, 100 and 130 kg/m^3 were used for the dynamic tests. These specimens were tested in out-of-plane configuration at two different strain rate levels (low and high dynamic).

3. Results and discussion

3.1. CMC and SDS-stabilized pulp fibre froth templates: Morphology and shape retention

Pulp fibre foams were prepared by frothing cellulose pulp fibres suspended in CMC and SDS solution. SDS served as a surfactant in the froths and CMC as a foam stabilizer. The addition of CMC led to a narrow bubble size distribution, and resulted in smaller bubbles throughout the wet froths (Fig. 1a). CMC was added to the formulation to increase the viscosity and as fibre–fibre adhesive. In the wet froth CMC prevents bubble coalescence and thus premature collapse of the foam structure during drying [44]. The foam density, and thus the porosity, is controlled by the amount of water and incorporated air into the froth. Fig. 1b shows optical micrographs of liquid froths: The froth solely stabilised by SDS had an inhomogeneous texture with clotted fibres and fewer and less well dispersed bubbles, while the froth also containing CMC had a smooth and homogeneous texture containing many bubbles separating the pulp fibres. SDS in conjunction with hydrophilic fibres lead to repulsion between fibres and air bubbles [19]. The viscosifying effect of CMC kinetically stabilised air bubbles and imparted

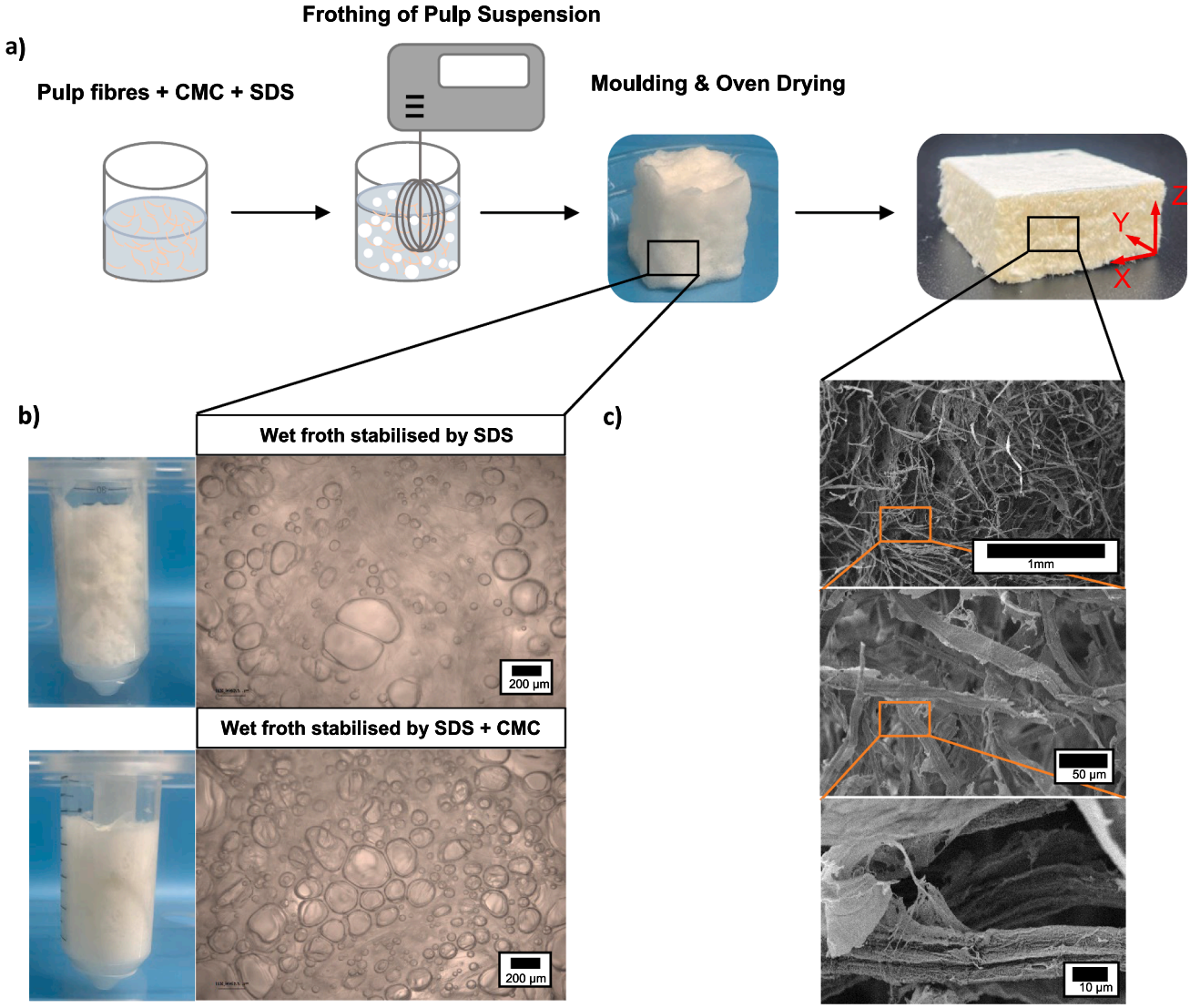

Fig. 1. A) schematic of pulp fibre froth preparation and morphology of wet froths and dry cellulose pulp fibre foams, b) optical micrographs showing the structure of wet pulp fibre froths stabilised solely with SDS (top), and SDS and CMC (bottom); c) scanning electron micrographs of pulp fibre foams produced by drying SDSand CMC stabilised froths showing the incorporation of CMC films in the 3D pulp fibre network.

dimensional stability to the wet froth, preventing drainage, bubble coalescence and allowing froth moulding. The half-lives of the air bubbles in the foam can be extended by the increased viscosity of the suspension caused by the addition of CMC, which provides improved colloidal stability.

Froth stability during drying is critical; high viscosity provided by CMC supports the structure and prevents collapse. Pöhler et al. [22] showed that the homogeneity of fibre foams can be tailored by polymeric additives; PVA addition resulted in the formation of more heterogeneous dry 3D fibre network structures when compared to the use of SDS alone as stabiliser. Drying of SDS-stabilised froths results in rapid froth collapse already during drainage, resulting in the formation of sheet-like porous pulp fibre structures, whereas SDS and CMC stabilised froths retain their structure during drying with minimal volume shrinkage of about 1 %. After moulding these froths can be transferred directly into an oven for drying. During drying, a densified skin layer (Fig. 1a right) forms on the open mould side, which slows water evaporation from bulk froth volume. The optimal CMC concentration in dry foams was determined to be 5 wt%. CMC forms films spanning fibres and likely bonding fibre joints. Increasing the CMC concentrations to 26 wt% resulted in the formation of lamellae between fibres in the 3D network and a lower form stability, i.e. higher shrinkage (~19 % – Figure S4). The increased froth stability due to the addition of CMC eliminated the need for post-processing to adjust the pulp foam density. We simply dispersed the desired fibre concentration in the suspension medium, which was sufficient to adjust the overall foam density. The porosity of the pulp fibre foams varied between 91 and 96 % (Table S5).

3.2. Morphological and structural analysis of pulp fibre foams via μCT

μCT was used to analyse the foam structure and to evaluate the fibre and pore orientation and distribution (Fig. 2a). The density distribution in the height direction (z) of pulp fibre foam was rather inhomogeneous (Fig. 2b). Local density minima were found in the region between 7 and 10 mm from the bottom, i.e. in the middle layer, for both high and low density foams. The bottom side had the target density (within error). In trough-thickness direction the density decreased towards the middle increasing again towards the top surface. The dense skin layer (Fig. 2b)

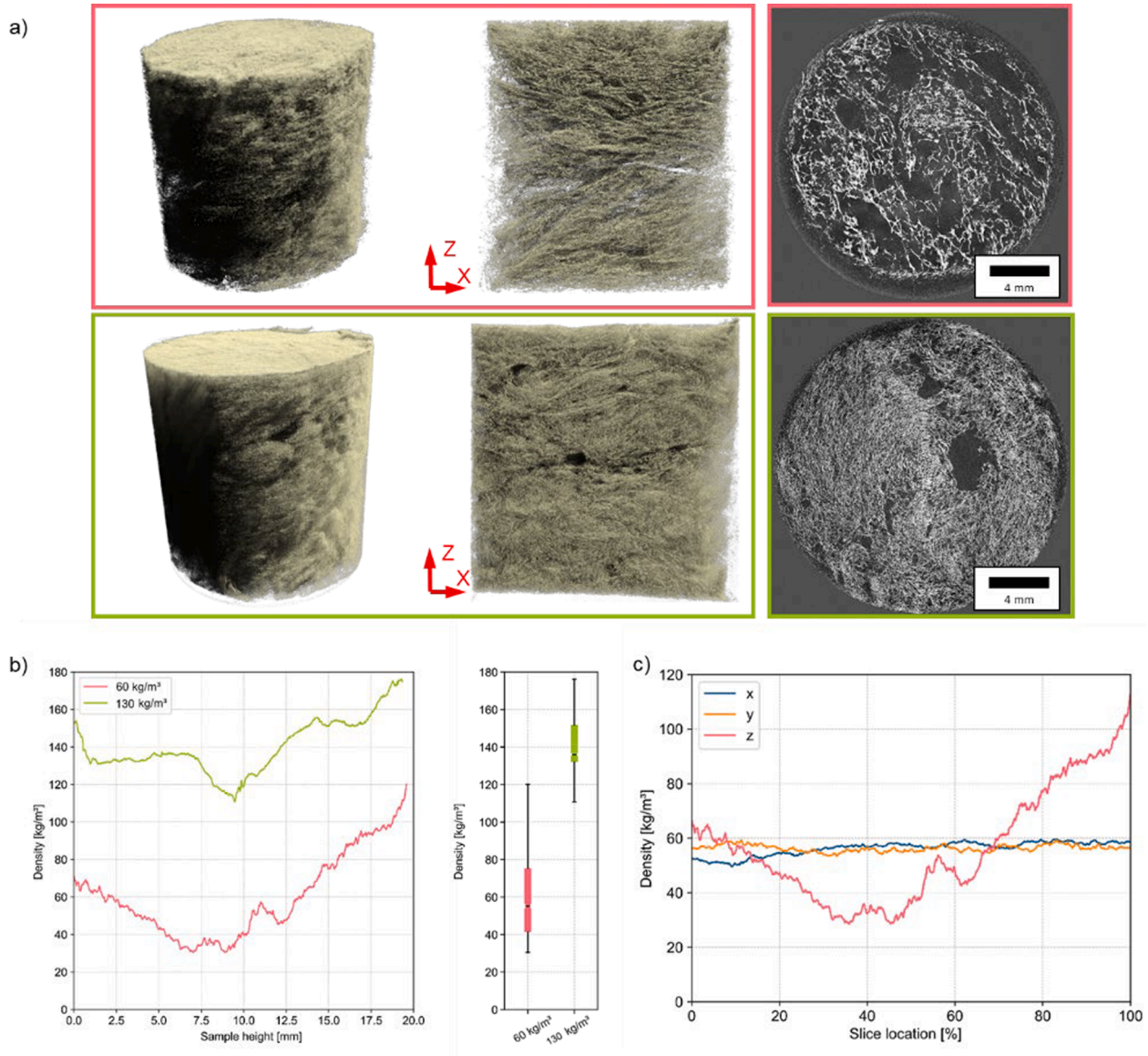

Fig. 2. A) μCT scans of pulp fibre foam (d = 20 mm, h = 20 mm), full view of 60 kg/m^3 specimen, cross-section of 60 kg/m^3 specimen,) μCT cross-section (xy-plane) of cellulose pulp fibre foams (up). full view of 130 kg/m^3 specimen, cross-section of 130 kg/m^3 specimen, μCT cross-section (xy-plane) of cellulose pulp fibre foams (below). b) comparison of density spread in z direction for a 60 kg/m^3 and a 130 kg/m^3 foam, c) Density distribution of a 60 kg/m^3 foam in x, y and z direction.

was confirmed on the open-mould side. Upon drying a denser layer, i.e. a skin, formed at the freely exposed surfaces due to higher drying rates in analogy to bread baking in which a crust forms within the first minutes [45]. Faster drying of wet froths results in the formation of a permeable yet insulating foam layer increasing the time required for drying [46]. Consequently, the froth dries in a heterogeneous manner, from outside to inside, resulting in different heating rates through the foam structure. The skin retains the shape of the froth in analogy to solidifying bread doughs [45]. Water removal occurs by either permeation, diffusion through the liquid phase or evaporation and diffusion through the gaseous phase [47]. In the wet froth, fibres were dispersed in the liquid foam phase and bubbles stabilised by CMC (Fig. 1b), forming films upon drying. The internal pressure in the froth increased as water is removed, causing the CMC-films to burst. The remnants of films can be seen in micrographs (Fig. 1c). CMC-film rupture caused pores to interconnect leading to an open porous heterogeneous foam structure (Fig. 1a right). Increasing the CMC content and thus the viscosity of the suspension medium resulted in thicker films stable enough to withstand the built-up of pressure resulting in a partly closed pore network (Figure S5). In the latter stages of drying, water evaporation slowed down as the outer layer become less porous. Combined with the increasing internal pressure due to increasing temperature and water vapour volume bubbles expand pushing fibres apart, leading to bigger pores in the foam interior promoting the formation of a heterogeneous foam structure. Fibre foams produced by draining prior to drying of froth stabilised by SDS alone exhibited a density gradient caused by fibre filtration [17,48].

Pulp fibre foams produced by drying frothed fibre suspensions containing CMC possessed a narrow density distribution in the xy-plane (Fig. 2b), thus suggesting a transversal isotropic density distribution. The density variation in the z direction reduced from 36.5 % to 11.1 % when increasing the foam density from 60 kg/m^3 to 130 kg/m^3, which is expected to affect compression, bending and shear behaviour, resulting in more isotropic foams that can be compared with expanded polystyrene (EPS) [49]and expanded polypropylene (EPP) [50].

The overall structure of pulp fibre foams is influenced by the bubble size distribution in wet froths. The foam density depends besides the water content on the amount of air incorporated into wet fibre froths. Air bubbles are entrapped between fibres in the viscous suspension medium. Al-Qararah et al. [51]showed that the homogeneity of the microstructure of foam-formed porous fibre materials of approximately the same envelop density depends on the Sauter mean pore diameter d_{32}; the larger the pore diameter the more heterogeneous the pore structure leading to decreased mechanical properties. Pore analysis of our foams showed that most pores had a rather small d_{32}. For foams with a nominal density of 60 kg/m^3 most pores had a d_{32} of about 0.6 mm and below (Figure S6a und b). Foams with a density of 130 kg/m^3 possess slightly larger pores with most exhibiting a d_{32} of about 0.7 mm. This observed trend toward larger pores in higher-density foams was attributed to more defined porosity and a shift toward a slightly more closed-cell structure, with clearer pores and a less random fibre distribution. As a result, higher-density foams contained more pronounced cell walls, which could accommodate larger pores. In contrast, lower-density foams exhibited a more random and loosely arranged fibre network resulting in smaller porosity, as voids created by the random arrangement of fibres, rather than gas bubbles, were also classified as pores in the applied analysis. The volume-weighted distribution was similar between the 60 kg/m^3 and 130 kg/m^3 foams, with a low content of small pores ($d_{32} \leq 0.15$ mm), followed by a steep increase in pore diameter occurrence until a peak was reached. After this peak, the number of larger pores gradually decreased, with only a few large pores ($d_{32} \geq 2$ mm) remaining. This represents a relatively broad distribution. Notably, slightly different results were observed for the maximum Feret diameter, where higher-density foams exhibited an even broader distribution. This suggested that the frothing process did not allow for homogeneous distribution of the incorporated air, leading to slightly larger and more elongated pores. The pore size distribution of pulp fibre foams was generally much broader (d_{32} from 30 μm up to about 3,000 μm) when compared to PU foams with similar densities containing pores in the range between 300–1,100 μm [52]. Larger pores are more prone to be elongated than smaller ones; so higher density foams with larger pores also exhibited a lower mean sphericity ($\Psi = 0.35$) as compared to foams with a lower density ($\Psi = 0.5$) (Figure S7), which is in agreement with the broader Feret diameter distribution. This is in contrast to polymer foams which exhibit pores with a higher mean sphericity of 0.7 and above [53]. The evaluation of the pore centroid distribution mirrors the results from the μCT-density analysis (Fig. 2c), showing more pores located in the middle of the specimen along the z direction, with little variance in the xy-plane (Figure S8). Fibre orientation analysis (Fig. 3) revealed that foams with 60 kg/m^3 density exhibited over 60 % of fibres with a zenithal fibre angle θ of 80° to 90°, meaning that most fibres were aligned in the xy-plane. Pulp fibre foams have a layered structure similar to paper products. Higher density foamss possessed a less severe, although still very pronounced in-plane orientation, with over 50 % of the fibres being oriented within 10° of the xy-plane. The in-plane φ angle distribution however was similar between foams of both densities, exhibiting an only slight preferred direction. It is assumed that this in-plane fibre orientation preference was induced by spreading the froths in the mould.

The pore orientation analysis (Figure S9) mirrored the trends shown Fig. 3, with fibres a predominant orientation in the xy-plane. Therefore, both the fibre and pore analyses indicate a level of orthotropic distribution as opposed to the transversal isotropic assumption. However, since the in-plane spread was negligible in relation to the overall scatter and the density distribution in the z direction a transversal isotropic assumption is justified. The μCT evaluation revealed the inhomogeneity of pulp fibre foams, which will affect their mechanical properties.

3.3. Mechanical properties of pulp fibre foams

3.3.1. Compression

Compression is the most critical load case for porous materials. Compression stress–strain curves of cellulose foams in out-of-plane orientation (load applied in z direction) are shown in Fig. 4. Pulp fibre foams with a density of less than 130 kg/m^3 do not exhibit a pronounced difference between the elastic and plateau regions. Instead, a single, almost linear elastic region was observed up to the densification strain ε_D. The absence of a defined plateau region, typically attributed to buckling behaviour in open and closed-cell synthetic foams [4], suggests that this mechanism has limited effect for low density pulp fibre foams when loaded out-of-plane. This behaviour is further supported by the low percentage of fibres oriented in the out-of-plane direction for low density foams (Fig. 3).

Noteworthy is the significant change in the materials response when evaluated in the in-plane direction (loading applied in the xy-plane). In this orientation, the pulp fibre foams exhibited a pronounced plateau region for all densities, though at relatively low levels (Fig. 4). The clear distinction between the initial elastic region and the plateau region, can be attributed to bending and buckling of numerous fibres, which were aligned in the (xy) plane as well as to the higher density skin layer. The in-plane Young's modulus E at equal density was over four times higher compared to the out-of-plane direction, in line with literature data [54]. The compression results obtained are presented in Table 1.

Gibson and Ashby [4] proposed approximations for the compression modulus E^* of open cell foams:

$$\frac{E^*}{E_S} = C_1 * \left(\frac{\rho^*}{\rho_s}\right)^2 \frac{E^*}{E_S} \approx \left(\frac{\rho^*}{\rho_s}\right)^2 \tag{10}$$

where E_s is the modulus of cellulose, C_1 a factor (of order 1), ρ* the envelope density of the foam and ρ_s the density of cellulose. The plateau strength σ^*_{pl} can be approximated by:

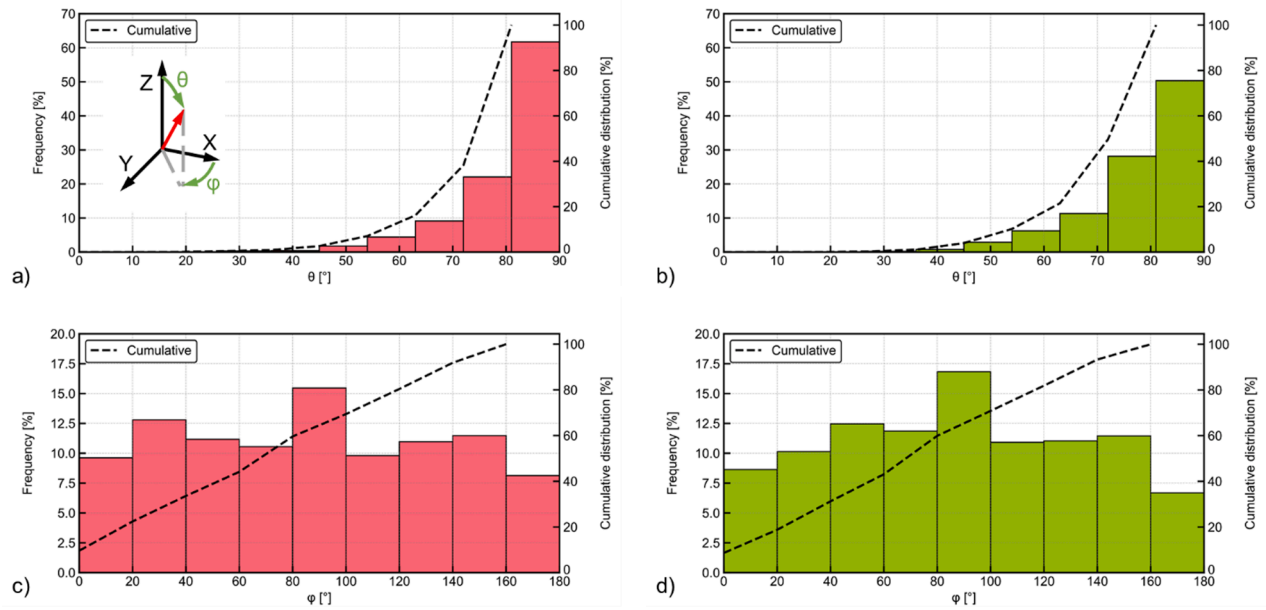

Fig. 3. A) out-of-plane fibre orientation distribution of a 60 kg/m^3 foam, b) out-of-plane fibre orientation distribution of a 130 kg/m^3 foam, c) in-plane fibre orientation distribution of a 60 kg/m^3 foam, d) in-plane fibre orientation distribution of a 130 kg/m^3 foam.

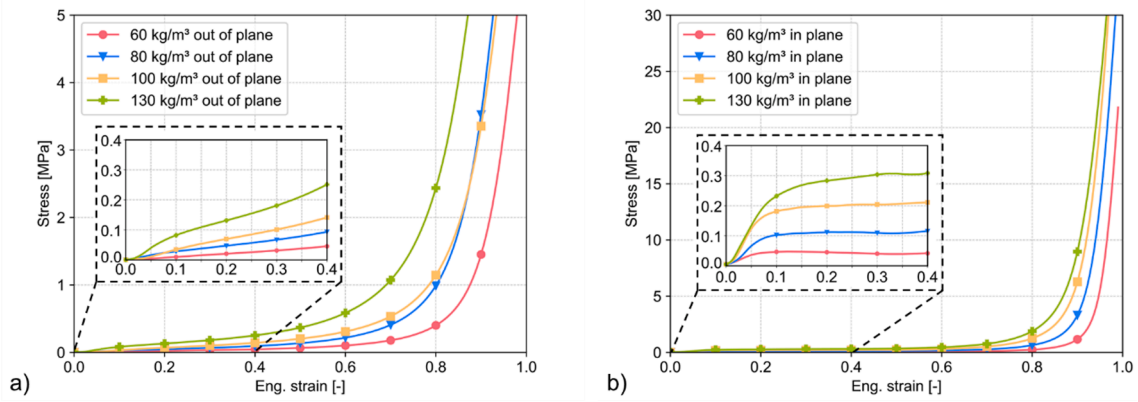

Fig. 4. A) mean out-of-plane stress strain curves for compression, b) mean in-plane stress strain curves for compression.

Table 1
Compression modulus E, mean crush strength $\overline{\sigma_c}$, compression strength at 10% densification strain $\sigma_{10\%}$, densification strain ε_D, specific energy absorption SEA of cellulose pulp fibre foams.

Specimen	ρ^* [kg/m^3]	E[kPa]	$\overline{\sigma_c}$[kPa]	$\sigma_{10\%}$[kPa]	ε_D [-]	SEA [J/g]
out-of-plane						
SC 1	60	74 ± 38	170	10 ± 3	0.91	1.04 ± 0.15
SC 2	80	300 ± 170	280	28 ± 10	0.87	1.70 ± 0.20
SC 3	100	190 ± 70	330	34 ± 15	0.86	2.00 ± 0.39
SC 4	130	780 ± 300	480	82 ± 16	0.81	2.95 ± 0.33
in-plane						
SC 5	60	620 ± 170	270	46 ± 8	0.95	0.94 ± 0.28
SC 6	80	1,220 ± 240	490	100 ± 20	0.93	1.68 ± 0.17
SC 7	100	2,350 ± 260	770	180 ± 10	0.92	2.47 ± 0.31
SC 8	130	2,560 ± 480	1,010	230 ± 40	0.92	3.02 ± 0.33

$$\frac{\sigma^*_{pl}}{\sigma_{ys}} \approx C_1 * \left(\frac{\rho^*}{\rho_s}\right)^{3/2} \tag{11}$$

where σ_{ys} is the yield strength and the proportionality factor C_1 can be approximated by 0.3. However, these equations did not accurately describe the compression properties of pulp fibre foams. The measured modulus and plateau strength were less than 10 % of the predicted values, when the softwood fibre elastic modulus is assumed to be 18 GPa and the yield strength is assumed to be 1 GPa (Table 2) [55]. Long spans between fibre–fibre connections, low buckling resistance of individual fibres or fibre–fibre debonding may contribute to the overall compressive behaviour not aligning with predictions. The densification strains

Table 2
Predicted modulus $E^*_{predicted}$, plateau strength $\sigma^*_{pl\_predicted}$, and densification strain $\varepsilon_{D\_predicted}$ of cellulose pulp fibre foams.

Density [kg/m^3]	$E^*_{predicted}$ [MPa]	$\sigma^*_{pl\_predicted}$ [MPa]	$\varepsilon_{D\_predicted}$ [-]
60	*28.8*	*2.4*	*0.94*
80	*51.2*	*3.7*	*0.93*
100	*80*	*5.2*	*0.91*
130	*135.2*	*7.7*	*0.88*

ε_D, however, are close to predicted values, with less than 10 % deviation between measured values and predicted ones:

$$\varepsilon_D \approx 1 - 1.4^{*}\frac{\rho^{*}}{\rho_s} \tag{12}$$

Fig. 5 displays a fitted power law for the compression modulus and $\sigma_{10\%}$ of pulp fibre foams as function of density. The exponent for the in-plane modulus function is 1.71 (±0.17), which correlates with a closed-cell foam structure, meaning that the modulus increases with density similarly to that in closed pore foams. The exponent in out-of-plane configuration is 3.16 (±0.45), which is associated with the presence of an open network structure [56], indicating that the fibre orientation has significant impact on the mechanical properties. Based on the in-plane exponent and the strong in-plane fibre orientation, it can be assumed that fibre buckling represents the dominant deformation mechanism in compression. This buckling behaviour might be similar to the buckling of struts and faces observed in closed-cell foams, suggesting a comparable underlying mechanism and, therefore,e a similar exponent. However, the overall stiffness and strength are low due to the limited connectivity within the fibre foams, likely contributing to the lower than expected proportional factor in the equation. The expected proportional factor should roughly equal E_s, while the determined proportional factor ranged between 1/10 x E_s and 1/100 x E_s. This explanation aligns with the higher exponent observed in the out-of-plane configuration, where fewer fibres were oriented along the loading path. Consequently, buckling is less dominant, and fibre bending and compression become more significant, leading to a higher exponent typically associated with fibrous networks. The fitted functions for in and out-of-plane moduli showed a good fit with an r^2 value over 0.75 while the fitted function for stress at 10 % strain showed even better correlation with an r^2 value over 0.9. These fitted functions can be used as the basis of most numerical simulation, and as opposed to discrete data points, enable easier density optimization for uniaxial compression load cases.

Fig. 6 places these resulting fitted material behaviour functions within the broader context of other cellulose-based foams. The out-of-plane properties agree fairly well with reported data for pulp fibre foams, while the in-plane properties are among the highest values documented for such foams. Micro- and nanofibrillated foams significantly outperform pulp fibre foams.

The compression properties of pulp fibre foams can be improved by crosslinking [57] or hydrolysing the cellulose pulp fibres [9]. However, crosslinking and hydrolysis of 3D networks of pulp fibres often involve harmful chemicals and negatively impact the biodegradability and sustainability aspects. In-plane measurements have shown the influence of the skin layer and fibre orientation in resisting compressive forces. Reichler et al.[50] designed a lightweight structure with intentionally dense skin layers, mimicking wood-like structures, and reported in-plane compression moduli up to 5.5 MPa while maintaining a density of only 50 kg/m^3. Ketola et al. [19]showed that the surfactant used to stabilise wet froths also influences the mechanical properties of pulp fibre foams. The choice of fibre and surfactant does affect fibre orientation; well bonded fibres in an anisotropic 3D random fibre network possess the highest strength (0.015 MPa) along the loading direction with the highest anisotropy. A closed cell pore structure forms when using smaller building blocks, such as CNF [58–60] or regenerated cellulose [61], which results in an isotropic structure able to distribute the applied stress more evenly resulting in much improved compression moduli and strengths. For similar pulp fibre foams with a density of 90 kg/m^3 and 161 kg/m^3 moduli of 460 kPa [62] and 1,100 kPa were reported [9], which aligns with our findings.

Comparing the moduli of our pulp fibre foams with conventional EPS foams of similar densities highlights their inferior compression properties. EPS foams with a density of 64 kg/m^3 have a modulus of 17.3 MPa, those of 80 kg/m^3 have similar moduli (18.3 MPa) while increasing the foam density further to 120 kg/m^3 results in significantly higher compression moduli of 51.8 MPa [72]. In contrast, the pulp fibre foams achieved only 0.5 to 4 % of the compression moduli reported for EPS. One advantageous property of fibre foams is their high densification strain of 0.8 to 0.95. In comparison to EPS foams, which have a densification strain of about 0.6 to 0.65, [50] pulp fibre foams can be compressed ~30 % further before they reach densification, which offers significant advantages in terms of energy absorption.

3.3.2. *Dynamic compression*

The quasi-static and dynamic compression stress–strain curves of pulp fibre foams with densities of 60, 100 and 130 kg/m^3 are shown in Fig. 7. A significant increase in compressive stress at any given strain was observed with increased strain rates (See Table 3). It is important to note that both the high dynamic and low dynamic curves terminate at lower strain values. This behaviour is inherent to Split Hopkinson pressure bar tests [42,43] when maintaining a constant specimen size; the achievable compression strain decreases with the applied loading speed.

Low density (60 kg/m^3) pulp fibre foams display a strain rate amplification factor of up to five, meaning that the strength at a given strain and strain rate is up to five times larger than in a quasi-static configuration. This is a significant increase of the strain-rate dependency compared to EPS foams with similar densities [73]. Increasing the density (130 kg/m^3) of pulp fibre foams seems to result in a strain rate amplification comparable to EPS foams (112 kg/m^3). The high strain rate sensitivity for low density pulp fibre foams proves particularly advantageous for energy absorption applications, such as for packaging and personal safety equipment. Furthermore, this data

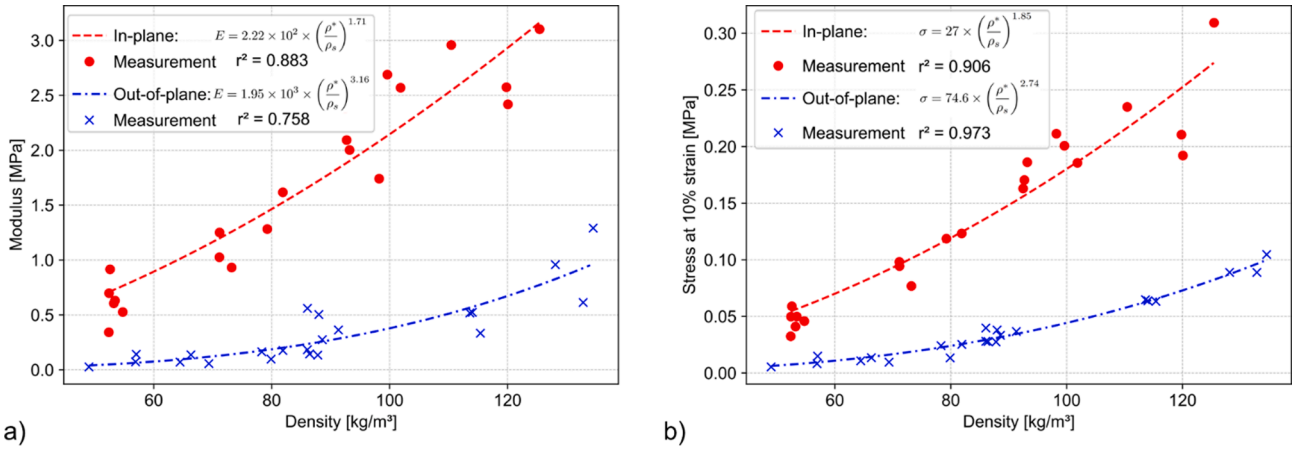

Fig. 5. A) modulus and b) stress at 10% strain fit function with respect to density, for the in-plane and out-of-plane compression cases of cellulose pulp fibre foams.

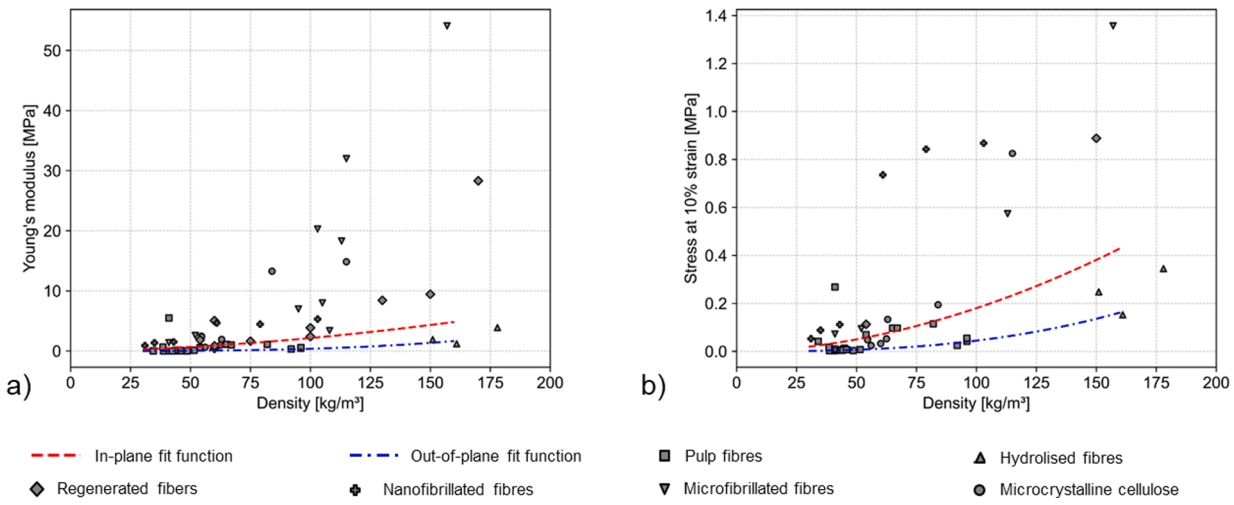

Fig. 6. A) modulus of fibre foams, b) stress at 10% strain references: pulp fibre foams[18,22,23,54,62–65]; Hydrolysed fibre foams [9]; Regenerated fibre foams [66,67]; Nanofibrillated fibre foams [60,68]; Microfibrillated fibre foams [54,69]; Microcrystalline cellulose foams [70,71].

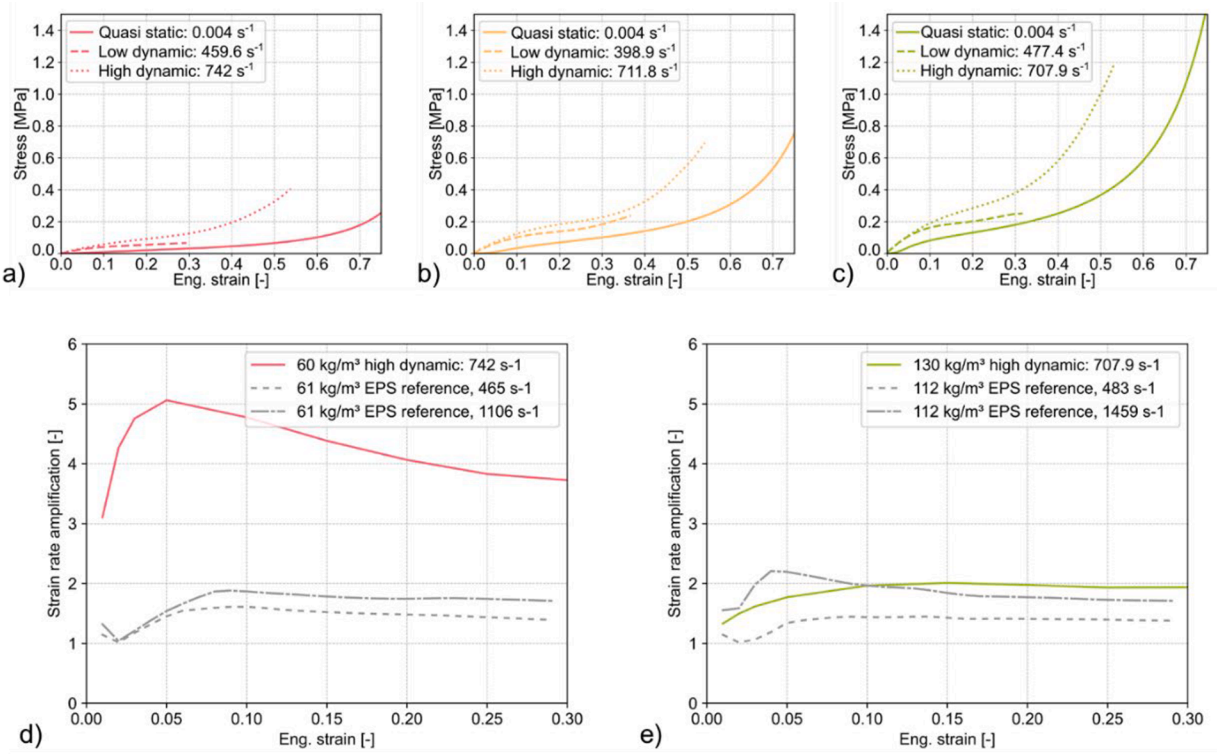

Fig. 7. Stress–strain curves of dynamic compression tests of a a) 60 kg/m^3 foam b) 100 kg/m^3 foam c) 130 kg/m^3 foam and strain rate amplification comparison between d) 60 kg/m^3 cellulose foam and 61 kg/m^3 EPS and e) 130 kg/m^3 foam and 112 kg/m^3 EPS.

Table 3
Mean crush strength σ_m at 25 % strain for 20 mm thick with low (400 – 500 1/s) and high dynamic (700 – 750 1/s) loading of cellulose pulp fibre foams.

Specimen	ρ^* [kg/m^3]	Strain rate [1/s]	σ_m[kPa]
SH 1 L	*60*	*460*	*62* ± 11
SH 1H	*60*	*742*	*107* ± 16
SH 2 L	*100*	*477*	*155* ± 27
SH 2H	*100*	*708*	*204* ± 45
SH 3 L	*130*	*399*	*225* ± 30
SH 3H	*130*	*712*	*326* ± 49

enables the utilization of strain rate dependent material models within numerical simulations such as models based on the constitutive law by Chang [74], which are essential for the adoption of materials in safety and energy absorption applications. While the high strain compression behaviour may not completely outweigh the limited compression properties, it substantially enhances the suitability of such foams for impact attenuation applications, as they become stronger with increasing loading rate, i.e. providing a load-rate adaptivity.

3.3.3. *Tension*

Tensile stress–strain curves of pulp fibre foams with varying densities are shown in Fig. 8a. The tensile strength in the xy-plane of pulp fibre foams decreases with decreasing density; however, the tensile strength

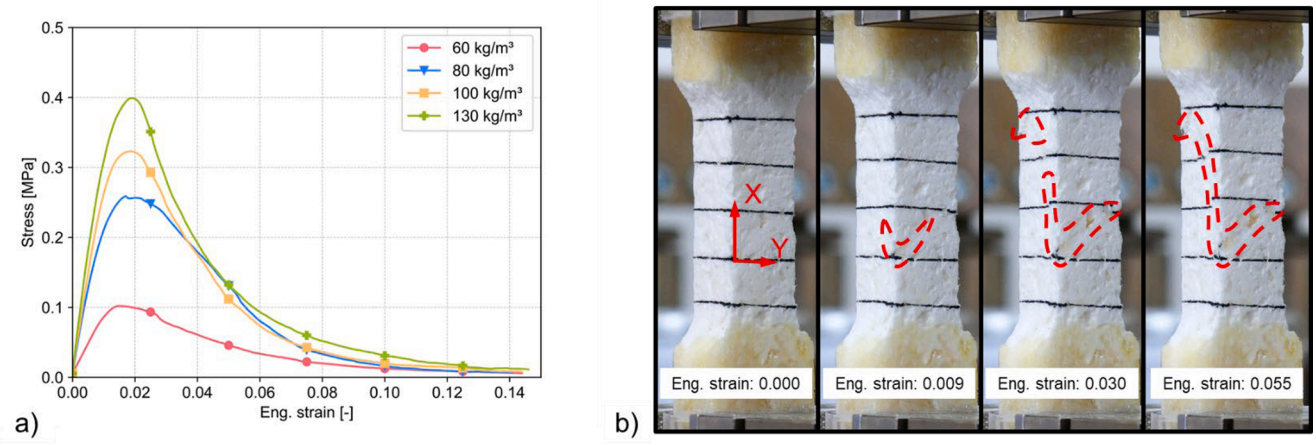

Fig. 8. A) mean tensile stress strain curves of pulp fibre foams with varying density. b) failure initiation and propagation until final failure of pulp fibre foams with a density of 130 kg/m^3.

of pulp fibre foams with a density of 60 kg/m^3 decreased much more significantly caused by the broad density distribution within these foams. The centre of the foam with a nominal density of 60 kg/m^3 had a density of only ~30 kg/m^3 and this was likely where the failure initiated (Fig. 8c). Presence of fines in pulp used to produce pulp fibre foams, such as CTMP, results in improve fibre–fibre bonding, which in turn was found to increase their tensile strength [17]. Skin layers provide a denser network and, therefore, higher network strength, which positively contributes to the tensile strength of pulp fibre foams. Tensile testing along the z-axis, as performed by Ketola et al. [19], showed that the z-strength is mainly influenced by the fibre orientation. In foams comprising a layered structure fewer fibre–fibre connections in z direction was observed. Generally, the tensile strength of the pulp fibre foams is much lower than that of synthetic polymer foams, though not as severely as their compression properties, with approximately 15 % of the tensile strength of EPP [75] and about 10 % compared to EPS [76].

Fig. 8b shows where the failure of the foams initiated. It is evident that local separations begin to occur at low strain levels (below 0.01). These localised separations, indicated by red lines, did occur in areas of the foam with minimal interconnectivity between fibres, attributed to density inhomogeneities. Following the initial appearance of these fractures, the tensile strength was reached at a strain of approximately 0.02 while fracture propagation continued until complete separation occurred up to strains of ~0.14. The failure strain of pulp fibre foams is between that of EPS and EPP foams. For instance, EPS have lower failure strains of ~0.04 to 0.05, [77,78] while EPP foams can exhibit failure strains ranging from 0.08 up to ~0.2 at room temperature [75,79]. Pulp fibre foams reach their peak tensile strength rather quickly until fully separated, whereas EPS and EPP fail shortly after reaching their tensile strength. This tensile fracture behaviour data is crucial for numerical modelling in safety applications, as it is essential for predicting failure and fracture.

3.3.4. Flexure

Under flexural loading (with force applied in z direction) all specimens exhibited tensile failure on the non-struck side, but no observable shear failure. The configuration in which the denser skin layer was loaded in tension surpassed the maximum forces compared to the samples in which the skin layer was under compression, except for the lowest density where the maximum force F_{max} (See Table 4) was relatively similar (Fig. 9a). The surface difference of the non struck side is shown in Fig. 9b and c. The observed behaviour is due to the dense skin layer offering additional strength in tension while potentially buckling and contributing less in compression. Pulp fibre foams with 60 kg/m^3 might not profit from the skin layer because of its lower density (Fig. 9a).

Pulp fibre foams exhibit a gradually decreasing flexural force until they fully fail (Fig. 9a), while EPS foams tend to fracture shortly after reaching their flexural strength, similar to the behaviour observed in tension [80].

Table 4
Peak force F_{max}, displacement at peak force s, modulus of rupture MOR and specific energy absorption at 40 mm displacement of cellulose pulp fibre foams.

Specimen	ρ^* [kg/m^3]	Struck side	F_{max} [N]	s [mm]	MOR [kPa]	SEA [mJ/g]
SB 1	*60*	*Skin*	*6.57* ± 0.54	*7.97*	*150* ± 12	*10.73* ± 1.32
SB 2	*60*	*No Skin*	*5.91* ± 0.14	*7.93*	*133* ± 3	*9.02* ± 1.58
SB 3	*80*	*Skin*	*11.19* ± 1.75	*8.23*	*252* ± 40	*10.06* ± 1.77
SB 4	*80*	*No Skin*	*13.37* ± 1.14	*13.56*	*301* ± 26	*20.54* ± 2.92
SB 5	*130*	*Skin*	*28.14* ± 2.47	*7.34*	*633* ± 56	*17.53* ± 1.39
SB 6	*130*	*No Skin*	*31.87* ± 3.31	*11.20*	*717* ± 74	*21.74* ± 8.90

3.3.5. Shear

Shear failure is the predominant core failure mode of foam materials in sandwich panel applications, underscoring the significance of this property for pulp fibre foams. Shear stress–strain curves are shown in Fig. 10. Similar to the behaviour observed in tension and flexural loading cases (Table 5), pulp fibre foams reached their peak strength relatively early, and the stress gradually decayed until full separation. Our tests were limited to out-of-plane shear properties, as this represents the most relevant load case for sandwich panel applications. Cellulose fibre foams with a density of 60 kg/m^3 achieve only about 14 % of the shear modulus reported for lower density (30 kg/m^3) EPS and merely 8 % of its shear strength $\tau_{xz\,max}$ [81]. For comparable EPS foam densities of 75 kg/m^3, the shear strength of pulp fibre foams is only 5 %. However, it is worth noting that limited shear data are available for comparable cellulose foams, even though such values are important for the design of possible sandwich structures and when modelling complex load cases.

3.4. Structure-density relation to mechanical properties

Fig. 11 illustrates the stiffness increase in compression, tension, and shear as a function of density, highlighting the sensitivity to both density and fibre orientation under various loading conditions. Most notable was the strong progressive trend observed for out-of-plane compression, which is explained by the increased initial density and the higher

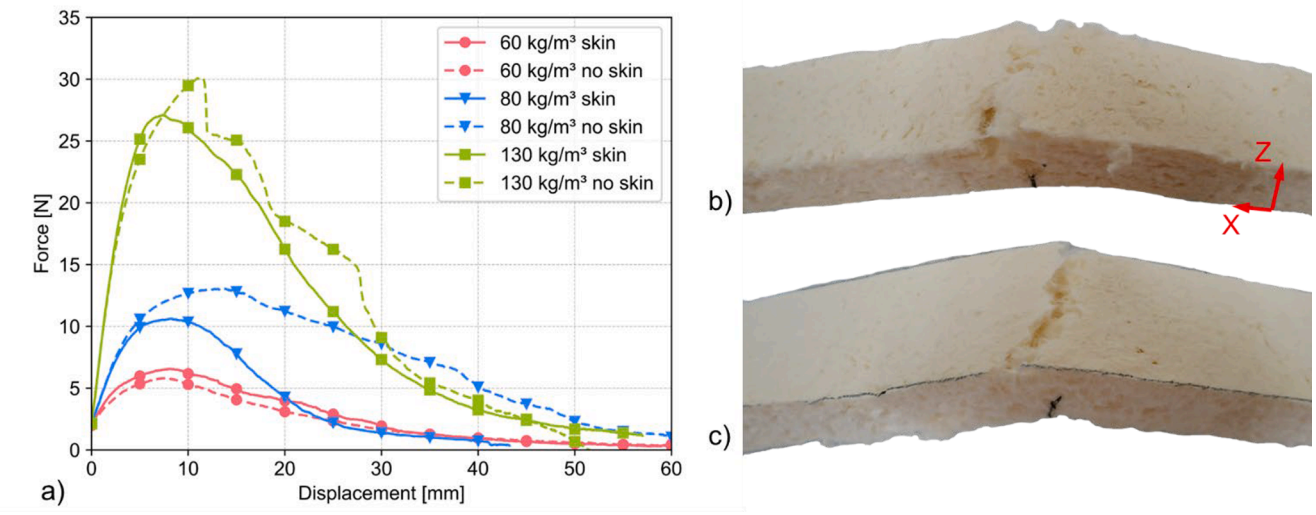

Fig. 9. A) mean three-point-bending force–displacement curves: b) skin struck side fracture c) no skin struck side fracture.

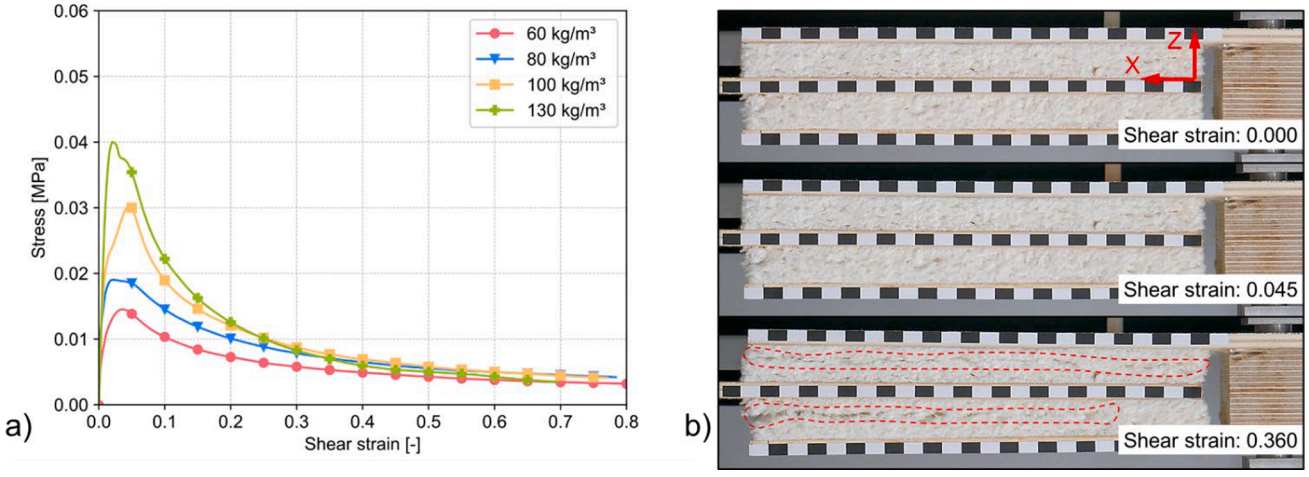

Fig. 10. A) mean shear stress over strain curves, b) fracture process of a 130 kg/m^3 shear specimen.

Table 5
Shear strength $\tau_{xz\,max}$ and shear modulus G of cellulose pulp fibre foams.

Specimen	ρ^* [kg/m^3]	τ_{xzmax} [kPa]	G[kPa]
SS 1	*60*	*18* ± 7	*820* ± 345
SS 2	*80*	*20* ± 3	*949* ± 169
SS 3	*100*	*31* ± 1	*1,182* ± 119
SS 4	*130*	*41* ± 7	*1,991* ± 418

percentage of fibres oriented in this direction with increased density. In contrast, the in-plane compressive stiffness shows only a slight progressive trend, resulting from the combination of increased initial density and the regressive effect of the lower percentage of fibres orientated in this direction. The shear stiffness also displays a progressive trend attributable to the increased percentage of fibres oriented out-of-plane which increased with increasing density, whereas low-density foams, with stronger in-plane orientation and layering, had less resistance to shear. Conversely, the in-plane tensile stiffness exhibits a regressive trend with increasing density, due to the lower percentage of fibres oriented in the in-plane direction.

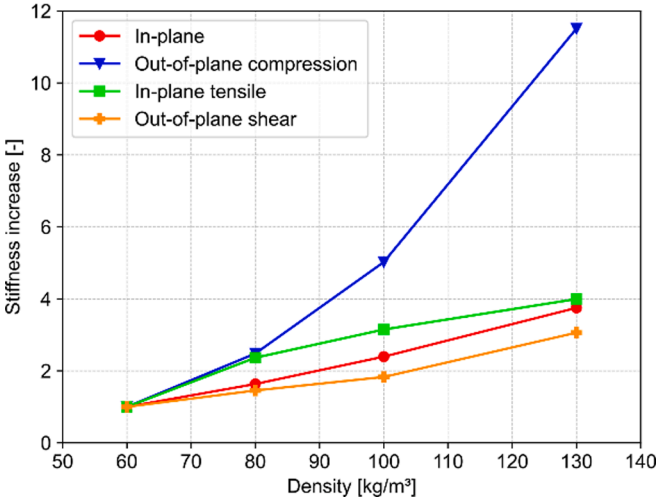

Fig. 11. Stiffness increase over density for compression, tension and shear loading.

4. Conclusion

This study offers a comprehensive mechanical and morphological analysis of cellulose fibre foams stabilized with SDS and CMC, highlighting their potential as eco-friendly alternatives to conventional polymer foams. The frothed foams demonstrated enhanced air bubble uniformity and dimensional stability, with shrinkage of less than 1 % upon drying. Density analysis revealed a pronounced gradient in the z-direction, with variations of up to 36.5 %, and the formation of skin layers on exposed surfaces during drying. Our results underscore the critical role of fibre orientation and density distribution on mechanical properties and suggest that optimizing fibre alignment could further enhance foam performance. Notably, over 50 % of the fibres were dispersed within 10° around the horizontal xy-plane, resulting in a pronounced anisotropy, where in-plane compressive strength and modulus where three times higher than those in the out-of-plane direction. The values in the out-of-plane direction are in good agreement with those reported in literature.

However, this strong in-plane orientation, i.e. this low spatial dispersion, adversely affects shear properties, indicating areas for future refinement. Moreover, we observed significant strain rate amplification, up to fivefold, in low-density pulp fibre foams, making them promising candidates for load-rate adapting applications, like in packaging and impact attenuation.

These findings lay a solid foundation for future research aimed at optimizing fibre orientation and structural design to further improve mechanical properties. Additionally, they support the development of predictive numerical models to enhance foam performance and drive progress in the use of sustainable materials.

CRediT authorship contribution statement

Markus Wagner: Writing – review & editing, Writing – original draft, Visualization, Validation, Software, Methodology, Investigation, Conceptualization. **Veronika Biegler:** Writing – review & editing, Writing – original draft, Visualization, Validation, Methodology, Investigation, Data curation, Conceptualization. **Sebastian Wurm:** Writing – review & editing, Validation, Investigation, Data curation. **Georg Baumann:** Writing – review & editing, Validation, Methodology, Investigation. **Tiina Nypelö:** Funding acquisition, Writing – review & editing, Conceptualization. **Alexander Bismarck:** Writing – review & editing, Project administration, Methodology, Conceptualization. **Florian Feist:** Writing – review & editing, Visualization, Supervision, Project administration, Methodology, Formal analysis, Conceptualization.

Declaration of competing interest

The authors declare that they have no known competing financial interests or personal relationships that could have appeared to influence the work reported in this paper.

Data availability

Data will be made available on request.

Acknowledgement

This work has received funding from the European Union's Horizon 2020 research and innovation programme under grant agreement No 964430.

Appendix A. Supplementary material

Supplementary data to this article can be found online at https://doi.org/10.1016/j.compositesa.2024.108515.

References

[1] Zhang W, Xu J. Advanced lightweight materials for Automobiles: A review. Mater Des 2022;221:110994.
[2] Fathi A, Wolff-Fabris F, Altstädt V, Gätzi R. An investigation on the flexural properties of balsa and polymer foam core sandwich structures: Influence of core type and contour finishing options. Jnl of Sandwich Struct & Mater 2013;15(5):487–508.
[3] Pollien A, Conde Y, Pambaguian L, Mortensen A. Graded open-cell aluminium foam core sandwich beams. Mater Sci Eng A 2005;404(1–2):9–18.
[4] Gibson LJ, Ashby MF. Cellular Solids 2014.
[5] Nechita P, Năstac SM. Overview on foam forming cellulose materials for cushioning packaging applications. Polymers 2022;14(10).
[6] Sarika PR, Nancarrow P, Khansaheb A, Ibrahim T. Progress in bio-based phenolic foams: synthesis, properties, and applications. ChemBioEng Rev 2021;8(6):612–32.
[7] Holt GA, Mcintyre G, Flagg D, Bayer E, Wanjura JD, Pelletier MG. Fungal mycelium and cotton plant materials in the manufacture of biodegradable molded packaging material: evaluation study of select blends of cotton byproducts. J Biobased Mat Bioenergy 2012;6(4):431–9.
[8] Semple KE, Zhou C, Rojas OJ, Nkeuwa WN, Dai C. Moulded pulp fibers for disposable food packaging: A state-of-the-art review. Food Packag Shelf Life 2022;33:100908.
[9] Ferreira ES, Rezende CA. Simple preparation of cellulosic lightweight materials from eucalyptus pulp. ACS Sustain Chem Eng 2018;6(11):14365–73.
[10] Pöhler T, Jetsu P, Fougerón A, Barraud V. Use of papermaking pulps in foam-formed thermal insulation materials. Nordic Pulp & Paper Research Journal 2017;32(3):367–74.
[11] Hjelt T, Ketoja JA, Kiiskinen H, Koponen AI, Pääkkönen E. Foam forming of fiber products: a review. J Dispers Sci Technol 2022;43(10):1462–97.
[12] Cucharero J, Ceccherini S, Maloney T, Lokki T, Hänninen T. Sound absorption properties of wood-based pulp fibre foams. Cellul 2021;28(7):4267–79.
[13] de Assis T, Pawlak J, Pal L, Jameel H, Venditti R, Reisinger LW, et al. Comparison of wood and non-wood market pulps for tissue paper application. BioRes 2019;14(3):6781–810.
[14] Ruska H, Kretschmer M. Übermikroskopische Untersuchungen über den Abbau von Zellulosefasern. Kolloid-Zeitschrift 1940;93(2):163–6.
[15] Ferreira ES, Rezende CA, Cranston ED. Fundamentals of cellulose lightweight materials: bio-based assemblies with tailored properties. Green Chem 2021;23(10):3542–68.
[16] Josset S, Orsolini P, Siqueira G, Tejado A, Tingaut P, Zimmermann T. Energy consumption of the nanofibrillation of bleached pulp, wheat straw and recycled newspaper through a grinding process. Nordic Pulp & Paper Research Journal 2014;29(1):167–75.
[17] Madani A, Zeinoddini S, Varahmi S, Turnbull H, Phillion AB, Olson JA, et al. Ultra-lightweight paper foams: processing and properties. Cellul 2014;21(3):2023–31.
[18] Ottenhall A, Seppänen T, Ek M. Water-stable cellulose fiber foam with antimicrobial properties for bio based low-density materials. Cellul 2018;25(4):2599–613.
[19] Ketola AE, Song W, Lappalainen T, Salminen K, Viitala J, Turpeinen T, et al. Changing the structural and mechanical anisotropy of foam-formed cellulose materials by affecting bubble-fiber interaction with surfactant. ACS Appl Polym Mater 2022;4(10):7685–98.
[20] He S, Liu C, Chi X, Zhang Y, Yu G, Wang H, et al. Bio-inspired lightweight pulp foams with improved mechanical property and flame retardancy via borate cross-linking. Chem Eng J 2019;371:34–42.
[21] Zheng C, Li D, Ek M. Cellulose-fiber-based insulation materials with improved reaction-to-fire properties. Nordic Pulp & Paper Research Journal 2017;32(3):466–72.
[22] Pöhler T, Ketoja JA, Lappalainen T, Luukkainen V-M, Nurminen I, Lahtinen P, et al. On the strength improvement of lightweight fibre networks by polymers, fibrils and fines. Cellul 2020;27(12):6961–76.
[23] Ketoja JA, Paunonen S, Jetsu P, Pääkkönen E. Compression strength mechanisms of low-density fibrous materials. Materials 2019;12(3).
[24] Bergström P, Hanson C, Ström H, Sasic S. Uniaxial compression of fibre networks – the synergetic effect of adhesion and elastoplasticity on non-reversible deformation. Powder Technol 2022;395:301–13.
[25] Sampson W. Unified theory for structural statistics of flocculated and random fibre networks. J Pulp Pap Sci 2008;34:91–8.
[26] Hollabaugh CB, Burt LH, Walsh AP. Carboxymethylcellulose. Uses and applications. Ind Eng Chem 1945;37(10):943–7.
[27] Laine J, Lindström T, Nordmark GG, Risinger G. Studies on topochemical modification of cellulosic fibres: Part 2. The effect of carboxymethyl cellulose attachment on fibre swelling and paper strength. Nordic Pulp & Paper Research Journal 2002;17(1):50–6.
[28] Blomstedt M, Kontturi E, Vuorinen T. Optimising CMC sorption in order to improve tensile stiffness of hardwood pulp sheets. Nordic Pulp & Paper Research Journal 2007;22(3):336–42.
[29] Pääkkönen E, Ketoja JA, Paltakari J. Energy absorption and resilience in quasi-static loading of foam-formed cellulose fibre materials. Cellul 2024;31(11):7137–52.
[30] Du Plessis A, Broeckhoven C, Guelpa A, Le Roux SG. Laboratory x-ray micro-computed tomography: a user guideline for biological samples. GigaScience 2017;6(6):1–11.
[31] Gostick J, Khan Z, Tranter T, Kok M, Agnaou M, Sadeghi M, et al. PoreSpy: a python toolkit for quantitative analysis of porous media images. JOSS 2019;4(37):1296.

[32] Gostick J, Aghighi M, Hinebaugh J, Tranter T, Hoeh MA, Day H, et al. OpenPNM: A pore network modeling package. Comput Sci Eng 2016;18(4):60–74.
[33] Gostick JT. Versatile and efficient pore network extraction method using marker-based watershed segmentation. Phys Rev E 2017;96(2–1):23307.
[34] Pons M-N, Vivier H, Delcour V, Authelin J-R, Paillères-Hubert L. Morphological analysis of pharmaceutical powders. Powder Technol 2002;128(2–3):276–86.
[35] van der Walt S, Schönberger JL, Nunez-Iglesias J, Boulogne F, Warner JD, Yager N, et al. scikit-image: image processing in Python. PeerJ 2014;2:e453.
[36] Frangi AF, Niessen WJ, Vincken KL, Viergever MA. Multiscale vessel enhancement filtering. In: Medical Image Computing and Computer-Assisted Intervention—MICCAI'98: First International Conference Cambridge, MA, USA, October 11–13, 1998 Proceedings 1. Springer Berlin Heidelberg; 1998. p. 130–7.
[37] Baranowski T, Dobrovolskij D, Dremel K, Hölzing A, Lohfink G, Schladitz K, et al. Local fiber orientation from X-ray region-of-interest computed tomography of large fiber reinforced composite components. Compos Sci Technol 2019;183:107786.
[38] Chen Y, Das R, Wang H, Battley M. Characterization of microstructures of SAN foam core using micro-computed tomography. Cell Polym 2021;40(4):143–64.
[39] Li QM, Magkiriadis I, Harrigan JJ. Compressive strain at the onset of densification of cellular solids. J Cell Plast 2006;42(5):371–92.
[40] Megson T. Bending of Open and Closed, Thin-Walled Beams:423–78.
[41] Mohanraj J, Barton DC, Ward IM, Dahoun A, Hiver JM, G'Sell C. Plastic deformation and damage of polyoxymethylene in the large strain range at elevated temperatures. Polymer 2006;47(16):5852–61.
[42] Chen W, Song B. Split Hopkinson (Kolsky) Bar. Boston, MA: Springer US; 2011.
[43] Baumann G, Czibula C, Hirn U, Feist F. A digital-twin driven Split Hopkinson bar layout for the tensile characterization of thin, low impedance, sheet-like materials. Int J Impact Eng 2024;194:105098.
[44] Interfacial Tension: Measurement;3:1.1-1.87.
[45] Jefferson DR, Lacey AA, Sadd PA. Understanding crust formation during baking. J Food Eng 2006;75(4):515–21.
[46] Keränen JT, Jetsu P, Turpeinen T, Koponen AI. Dewatering and structural analysis of foam-formed, lightweight fibrous materials. BioRes 2023;18(1):531–49.
[47] Zhang L, Doursat C, Vanin FM, Flick D, Lucas T. Water loss and crust formation during bread baking, Part I: Interpretation aided by mathematical models with highlights on the role of local porosity. Drying Technol 2017;35(12):1506–17.
[48] Lecourt M, Pöhler T, Hornatowska J, Salmén L, Jetsu P. Density profiles of novel kraft pulp and TMP based foam formed thermal insulation materials observed by X-ray tomography and densitometry. Holzforschung 2018;72(5):397–403.
[49] Mosleh Y, Vanden Bosche K, Depreitere B, Vander Sloten J, Verpoest I, Ivens J. Effect of polymer foam anisotropy on energy absorption during combined shear-compression loading. J Cell Plast 2018;54(3):597–613.
[50] Xing Y, Sun D, Zhang M, Shu G. Crushing responses of expanded polypropylene foam. Polymers 2023;15(9).
[51] Al-Qararah AM, Ekman A, Hjelt T, Ketoja JA, Kiiskinen H, Koponen A, et al. A unique microstructure of the fiber networks deposited from foam–fiber suspensions. Colloids Surf A Physicochem Eng Asp 2015;482:544–53.
[52] Zhang C, Li J, Hu Z, Zhu F, Huang Y. Correlation between the acoustic and porous cell morphology of polyurethane foam: Effect of interconnected porosity. Mater Des (1980–2015) 2012;41:319–25.
[53] Kosmela P, Suchorzewski J, Formela K, Kazimierski P, Haponiuk JT, Piszczyk Ł. Microstructure-Property relationship of polyurethane foams modified with baltic sea biomass: microcomputed tomography vs scanning electron microscopy. Materials 2020;13(24).
[54] Reichler M, Rabensteiner S, Törnblom L, Coffeng S, Viitanen L, Jannuzzi L, et al. Scalable method for bio-based solid foams that mimic wood. Sci Rep 2021;11(1):24306.
[55] Neto J, Queiroz H, Aguiar R, Lima R, Cavalcanti D, Doina BM. A review of recent advances in hybrid natural fiber reinforced polymer composites. J Renew Mater 2022;10(3):561–89.
[56] Lavoine N, Bergström L. Nanocellulose-based foams and aerogels: processing, properties, and applications. J Mater Chem A 2017;5(31):16105–17.
[57] Wu M, Yu G, Chen W, Dong S, Wang Y, Liu C, et al. A pulp foam with highly improved physical strength, fire-resistance and antibiosis by incorporation of chitosan and CPAM. Carbohydr Polym 2022;278:118963.
[58] Jiang F, Hsieh Y-L. Amphiphilic superabsorbent cellulose nanofibril aerogels. J Mater Chem A 2014;2(18):6337–42.
[59] Sehaqui H, Zhou Q, Berglund LA. High-porosity aerogels of high specific surface area prepared from nanofibrillated cellulose (NFC). Compos Sci Technol 2011;71(13):1593–9.
[60] Kobayashi Y, Saito T, Isogai A. Aerogels with 3D ordered nanofiber skeletons of liquid-crystalline nanocellulose derivatives as tough and transparent insulators. Angew Chem Int Ed Engl 2014;53(39):10394–7.
[61] Malekzadeh H, Md Zaid NSB, Bele E. Characterization and structural properties of bamboo fibre solid foams. Cellul 2021;28(2):703–14.
[62] Ferreira ES, Cranston ED, Rezende CA. Naturally hydrophobic foams from lignocellulosic fibers prepared by oven-drying. ACS Sustain Chem Eng 2020;8(22):8267–78.
[63] Lazzari LK, Zampieri VB, Neves RM, Zanini M, Zattera AJ, Baldasso C. A study on adsorption isotherm and kinetics of petroleum by cellulose cryogels. Cellul 2019;26(2):1231–46.
[64] Burke SR, Möbius ME, Hjelt T, Hutzler S. Properties of lightweight fibrous structures made by a novel foam forming technique. Cellul 2019;26(4):2529–39.
[65] López Durán V, Erlandsson J, Wågberg L, Larsson PA. Novel, cellulose-based, lightweight, wet-resilient materials with tunable porosity, density, and strength. ACS Sustain Chem Eng 2018;6(8):9951–7.
[66] Wan C, Lu Y, Jiao Y, Cao J, Sun Q, Li J. Preparation of mechanically strong and lightweight cellulose aerogels from cellulose-NaOH/PEG solution. J Sol-Gel Sci Technol 2015;74(1):256–9.
[67] Sescousse R, Gavillon R, Budtova T. Aerocellulose from cellulose–ionic liquid solutions: Preparation, properties and comparison with cellulose–NaOH and cellulose–NMMO routes. Carbohydr Polym 2011;83(4):1766–74.
[68] Sehaqui H, Salajková M, Zhou Q, Berglund LA. Mechanical performance tailoring of tough ultra-high porosity foams prepared from cellulose I nanofiber suspensions. Soft Matter 2010;6(8):1824.
[69] Svagan AJ, Berglund LA, Jensen P. Cellulose nanocomposite biopolymer foam–hierarchical structure effects on energy absorption. ACS Appl Mater Interf 2011;3(5):1411–7.
[70] Ganesan K, Dennstedt A, Barowski A, Ratke L. Design of aerogels, cryogels and xerogels of cellulose with hierarchical porous structures. Mater Des 2016;92:345–55.
[71] Ganesan K, Barowski A, Ratke L, Milow B. Influence of hierarchical porous structures on the mechanical properties of cellulose aerogels. J Sol-Gel Sci Technol 2019;89(1):156–65.
[72] Ling C, Cardiff P, Gilchrist MD. Mechanical behaviour of EPS foam under combined compression-shear loading. Mater Today Commun 2018;16:339–52.
[73] Ouellet S, Cronin D, Worswick M. Compressive response of polymeric foams under quasi-static, medium and high strain rate conditions. Polym Test 2006;25(6):731–43.
[74] Chang FS, Song Y, Lu DX, DeSilva CN. Unified constitutive equations of foam materials. J Eng Mater Technol 1998;120(3):212–7.
[75] Lee YS, Park NH, Yoon HS. Dynamic mechanical characteristics of expanded polypropylene foams. J Cell Plast 2010;46(1):43–55.
[76] Di Landro L, Sala G, Olivieri D. Deformation mechanisms and energy absorption of polystyrene foams for protective helmets. Polym Test 2002;21(2):217–28.
[77] Doroudiani S, Kortschot MT. Polystyrene foams. III. Structure–tensile properties relationships. J of Applied Polymer Sci 2003;90(5):1427–34.
[78] Chen W, Hao H, Hughes D, Shi Y, Cui J, Li Z-X. Static and dynamic mechanical properties of expanded polystyrene. Mater Des (1980–2015) 2015;69:170–80.
[79] Weingart N, Raps D, Kuhnigk J, Klein A, Altstädt V. Expanded polycarbonate (EPC)-A new generation of high-temperature engineering bead foams. Polymers 2020;12(10).
[80] Lu Z, Jónsdóttir F, Arason S, Margeirsson B. Assessment of compressive and flexural properties and stacking strength of expanded polystyrene boxes: experimental and simulation study. Appl Sci 2023;13(10):5852.
[81] Vejelis S, Gnip I, Vaitkus S, Keršulis V. Shear strength and modulus of elasticity of expanded polystyrene (EPS). Medziagotyra 2008;14:230–3.